PERGAMON

International Journal of Heat and Mass Transfer 41 (1998) 3279–3298

International Journal of HEAT and MASS TRANSFER

Convective flow and heat transfer in a channel containing multiple heated obstacles

Timothy J. Young[1], Kambiz Vafai*

Department of Mechanical Engineering, The Ohio State University, Columbus, OH 43210, U.S.A.

Received 28 May 1997; in final form 3 December 1997

Abstract

The present work details the numerical simulation of forced convective, incompressible flow in a channel with an array of heated obstacles attached to one wall. Three levels of Nusselt numbers are emphasized in this systematic analysis: local distributions along the obstacle exposed faces, mean values for individual faces, and overall obstacle mean values. This study details the effects of variations in the obstacle height, width, spacing, and number, along with the obstacle thermal conductivity, fluid flow rate, and heating method, to illustrate important fundamental and practical results. The periodicity of the mean Nusselt number is established, relative to the ninth obstacle, at the 5% and 10% difference levels (eighth and seventh obstacles, respectively). The periodic behavior of the velocity components and temperature distributions are also explicitly demonstrated for the array. Extensive presentation and evaluation of the mean Nusselt numbers for all obstacles within the array is fully documented. The results pave the way for different applications involving multiple heated obstacles.

Nomenclature

A, B, C, D obstacle corners
c_p specific heat at constant pressure [J (kg·K)$^{-1}$]
D_h hydraulic diameter [m]
h obstacle height [m]
h_c convective heat transfer coefficient [W (m^2·K)$^{-1}$]
H channel height [m]
k thermal conductivity [W (m·K)$^{-1}$]
L length [m]
n normal coordinate
Nu Nusselt number $[h_c H/k_f]$
p pressure [Pa]
Pe_H Péclect number $[\rho_f c_{p_f} u_m H/k_f]$
Pr Prandtl number $[\mu_f c_{p_f}/k_f]$
q'' heat flux [W m^{-2}]
q''' volumetric heat generation rate [W m^{-3}]
Re_H Reynolds number $[\rho_f u_m H/\mu_f]$
s obstacle spacing [m]
T temperature [K]
u x-component of velocity [m s^{-1}]
v y-component of velocity [m s^{-1}]
w obstacle width [m]
x, y Cartesian coordinates.

Greek symbols
μ dynamic viscosity [(N·s) m^{-2}]
Θ dimensionless temperature $[(T-T_c)/(q''H/k_f)]$
ρ density [kg m^{-3}].

Subscripts
f fluid
e entrance
L left surface (**AB**)
m mean
o outlet
R right surface (**CD**)
s solid
T top surface (**BC**)
w wall
x local.

Superscripts
* dimensionless
¯ mean.

* Corresponding author.
[1] Current address: Aerospace Power Division, WL/POOD, 1950 Fifth St, WPAFB, OH 45433-7251, U.S.A.

0017–9310/98 $19.00
PII: S0017-9310(98)00014-3

1. Introduction

The fluid flow in a channel containing heated obstacles has been of interest for several decades as the canonical model for electronic component cooling. Both experimental and numerical methods have been employed, as detailed by Peterson and Ortega [1], to study a wide variety of problems. These include two- and three-dimensional systems in laminar or turbulent flow with natural, mixed, or forced convection. The powered components are generally idealized as quadrilateral obstacles mounted individually or in arrays to a channel wall with thermal energy transfer to the surroundings. Improved thermal design of electronic components is necessary to reduce hot spots, increase energy throughput, and reduce the failure rate, which is related to the device junction temperature.

The two-dimensional, conjugate heat transfer problem for laminar flow over an array of three obstacles was solved, utilizing a control volume formulation, by Davalath and Bayazitoglu [2]. Their obstacles had uniform conductivity and were volumetrically heated. The spacing between the obstacles was varied from one to two times the obstacle width. Their analysis included the effects of obstacle spacing on the maximum temperature attained within the obstacles and the development of overall mean Nusselt number correlations of the form $\overline{Nu}_m = aRe^b\,Pr^c$ for the obstacles.

The mixed convective flow around three obstacles, in both horizontal and vertical channels, was numerically studied by Kim *et al.* [3]. The planar heat sources were situated near the obstacle mid-height while the geometries were fixed. Special consideration was given, using cross-stream periodic boundary conditions, to account for conductive channel walls. Detailed local Nusselt number distributions for various Gr/Re^2 were presented, showing greater heat transfer at the first obstacle and decreasing over the two downstream obstacles.

The buoyancy enhanced laminar flow over three obstacles in a vertical channel was investigated by Kim and Boehm [4]. The obstacle surfaces and channel wall upon which they were attached was kept isothermal while the facing wall was insulated. Using a finite element method, total mean Nusselt numbers were found, along with velocity and temperature profiles across the channel. Experimental measurements of mean Nusselt numbers and thermal wake functions were made for 5 column by 21 row array of low profile obstacles, with only the first 10 rows heated, by Lehmann and Pembroke [5]. The square cross section obstacles had a large width to height ratio (~ 17) and were closely spaced. Variations in channel spacing and flow rate were made. The obstacle mean Nusselt numbers were found to be largest at the first row and decrease to nearly row-independent values by the third row. Similar $\overline{Nu}_m$ versus row effects were also found in the experimental investigation of a 5 column by 8 row obstacle array by Jubran et al. [6].

The work of Huang and Vafai [7] is of particular relevance to the multiple obstacle configuration. The enhancement of forced convective flow and thermal characteristics using various arrangements of multiple porous obstacles in a channel was demonstrated. The Brinkman–Forchheimer-extended Darcy model was used to fully account for boundary and inertial effects within the porous obstacles. The use of the porous obstacles enhanced the mixing within the fluid region resulting in much higher heat transfer than for the corresponding smooth channel. Substantial periodicity, control of vortices, and large increases in Nusselt number were shown through alteration of governing physical parameters.

This work presents a systematic and thorough investigation of forced convective cooling of a two-dimensional array of multiple heated obstacles located upon one wall of an insulated channel. The baseline case has five obstacles heated at their bases by a surface flux. The influences of parametric changes in the obstacle geometry, spacing, number, thermal conductivity, and heating method, at various flow rates, upon the flow and heat transfer are examined to establish important fundamental effects and provide practical results. The dependence of the streamlines, isotherms, and Nusselt numbers on the governing parameters is documented. Local Nusselt number distributions and mean Nusselt numbers for the individual exposed obstacle faces are given particular emphasis. The validity of periodic boundary conditions for arrays of obstacles is explicitly evaluated, through both mean and local characteristics, at both the 5% and 10% difference levels. It is shown that specific choices in certain governing parameters, such as obstacle height or spacing, can make significant changes in the cooling of the obstacles, whereas others, such as heating method, exert little influence.

2. Analysis

The flow through the two-dimensional channel is assumed to be represented by a steady, incompressible, Newtonian fluid. Buoyancy effects are assumed negligible, as are those of viscous heat dissipation. The thermophysical properties of the fluid and the solid obstacles are taken as constant. The governing fluid phase equations expressing the conservation of mass, x- and y-momentum, and energy, in Cartesian coordinates, are, respectively,

$$\frac{\partial u^*}{\partial x^*} + \frac{\partial v^*}{\partial y^*} = 0 \tag{1}$$

$$Re_H\left(u^*\frac{\partial u^*}{\partial x^*} + v^*\frac{\partial u^*}{\partial y^*}\right) = -\frac{\partial p^*}{\partial x^*} + \left(\frac{\partial^2 u^*}{\partial x^{*2}} + \frac{\partial^2 u^*}{\partial y^{*2}}\right) \tag{2}$$

$$Re_H\left(u^*\frac{\partial v^*}{\partial x^*} + v^*\frac{\partial v^*}{\partial y^*}\right) = -\frac{\partial p^*}{\partial y^*} + \left(\frac{\partial^2 v^*}{\partial x^{*2}} + \frac{\partial^2 y^*}{\partial y^{*2}}\right) \tag{3}$$

$$Pe_H\left(u^*\frac{\partial\Theta_f^*}{\partial x^*}+v^*\frac{\partial\Theta_f^*}{\partial y^*}\right)=\frac{\partial^2\Theta_f^*}{\partial x^{*2}}+\frac{\partial^2\Theta_f^*}{y^{*2}}. \quad (4)$$

The thermal energy release in an electronic component can be approximated as a constant surface heat flux or as volumetric generation. Both of these approaches have been utilized in previous numerical and experimental investigations. The energy equation for the solid phase, accounting for a volumetric source term, is

$$\left(\frac{k_s}{k_f}\right)\left(\frac{\partial^2\Theta_s}{\partial x^2}+\frac{\partial^2\Theta_s}{\partial y^2}\right)+\vartheta q'''=0 \quad (5)$$

where $\vartheta=0$ when a surface heat flux is applied to the obstacle and $\vartheta=1$ for volumetric heat generation. In order to equalize the total energy input into the obstacles, the energy source terms were balanced as $q''w=q'''wh$, where q'' is the applied surface heat flux when $\vartheta=0$ and q''' is the volumetric heat generation when $\vartheta=1$.

The governing equations were cast into dimensionless form using the following

$$u^*\equiv\frac{u}{u_m},\quad v^*\equiv\frac{v}{u_m},\quad x^*\equiv\frac{x}{H},\quad y^*\equiv\frac{y}{H},\quad p^*\equiv\frac{pH}{\mu_f u_m}$$

$$\Theta\equiv\frac{T-T_e}{q''H/k_f},\quad Re_H\equiv\frac{\rho_f u_m H}{\mu_f},\quad Pe_H\equiv\frac{\rho_f c_p u_m H}{k_f}. \quad (6)$$

The mean velocity is calculated from $u_m=H^{-1}\int_0^H u\,dy$. The dimensionless obstacle height, width, and spacing are given, respectively, by $h^*\equiv h/H$, $w^*\equiv w/H$, and $s^*\equiv s/H$ as shown in Fig. 1(a). The obstacle faces are designated, for example, as **AB**, corresponding to the surface between corners **A** and **B**. The obstacle thermal conductivity is k_s/k_f, i.e. it is nondimensionalized with respect to the fluid thermal conductivity. Further use of the superscripts is suppressed.

To assess the effects of the changes in governing parameters on the obstacle heat transfer, the local Nusselt number is evaluated as

$$Nu_x=\frac{h_c H}{k_f}=\frac{-1}{\Theta_w}\frac{\partial\Theta_f}{\partial\mathbf{n}} \quad (7)$$

where the temperature gradient at the wall is calculated using a three-point finite difference. The mean values of the Nusselt number for the three exposed faces **AB**, **BC**, and **CD** ($\overline{Nu}_L$, $\overline{Nu}_T$, $\overline{Nu}_R$), and the overall obstacle mean ($\overline{Nu}_m$), are calculated using

$$\overline{Nu}_i=\frac{\int_{A_i}Nu_x\,dx}{A_i}\quad\text{and}\quad\overline{Nu}_m=\frac{\sum_{i=L,T,R}\overline{Nu}_i A_i}{A_L+A_T+A_R} \quad (8)$$

where A_i is the overall exposed area of the obstacle. The overall obstacle mean value is thus an area weighted average of the exposed face mean values.

2.1. Boundary conditions

Boundary conditions along the entire solution domain must be specified for all field variables due to the elliptic nature of the governing conservation equations. At the inlet to the channel a fully developed, parabolic velocity profile is specified. At the outlet the streamwise gradients of the velocity components are assumed to be zero. The implication is that the flow is nearly fully developed at the exit plane. Furthermore, by choosing an extended computational domain it was ensured that the computational outflow boundary conditions had no effect upon the physical domain solution (Vafai and Kim [8]). This process is explained in more detail below.

The fluid, at the entrance, is assumed to be at the ambient temperature. At the outlet the temperature gradient in the axial direction is set to zero. Again, the choice of an extended computational domain ensured that the thermal boundary condition at the exit had no significant effect upon the solution near the region of interest. The solid obstacles, for the baseline case, receive a constant heat flux at their base, face **AD**. At the fluid–solid interfaces, faces **AB**, **BC**, and **CD**, the no-slip condition and the continuities of temperature and heat flux are taken into account. The channel walls are insulated except at the obstacle locations. This condition was selected to illustrate the significant aspects of parametric changes in the heated obstacles to the flow and thermal fields. Though isothermal or adiabatic wall conditions simplify the heat transfer from powered devices to the coolant and circuit boards [3], conjugate modeling creates a more system specific problem that may obscure relevant underlying details. In summary, the boundary conditions are described in the following dimensionless form.

1. At the entrance ($x=0, 0\leqslant y\leqslant 1$)

$$u=6y(1-y),\quad v=0,\quad \Theta_f=0. \quad (9)$$

2. At the outlet

($x=L_c+N_t w+(N_t-1)s+L_o,\quad 0\leqslant y\leqslant 1$)

$$\frac{\partial u}{\partial x}=0,\quad\frac{\partial v}{\partial x}=0,\quad\frac{\partial\Theta_f}{\partial x}=0. \quad (10)$$

3. Along the obstacle bases, **AD**, ($L_e+(N-1)(w+s)\leqslant x\leqslant L_e+Nw+(N-1)s, y=0$) the prescribed heat flux is $q''=1$.

4. Along the fluid/solid interfaces (**AB**, **BC**, **CD**)

$$u=0,\quad v=0,\quad\Theta_f=\Theta_s,\quad k_f\frac{\partial\Theta_f}{\partial\mathbf{n}}=k_s\frac{\partial\Theta_s}{\partial\mathbf{n}}. \quad (11)$$

5. Along the bottom channel wall, where $y=0$ and

$$0\leqslant x<L_e$$

$$L_e+Nw+(N-1)s<x<L_e+N(w+s)$$

$$L_e+N_i w+(N_t-1)s<x\leqslant L_e+N_t w+(N_t-1)s+L_o$$

and on the upper channel wall ($0\leqslant x\leqslant L_e+N_t w+(N_t-1)s+L_o, y=1$) the following boundary conditions are applied.

$$u=0,\quad v=0,\quad\frac{\partial\Theta_f}{\partial y}=0. \quad (12)$$

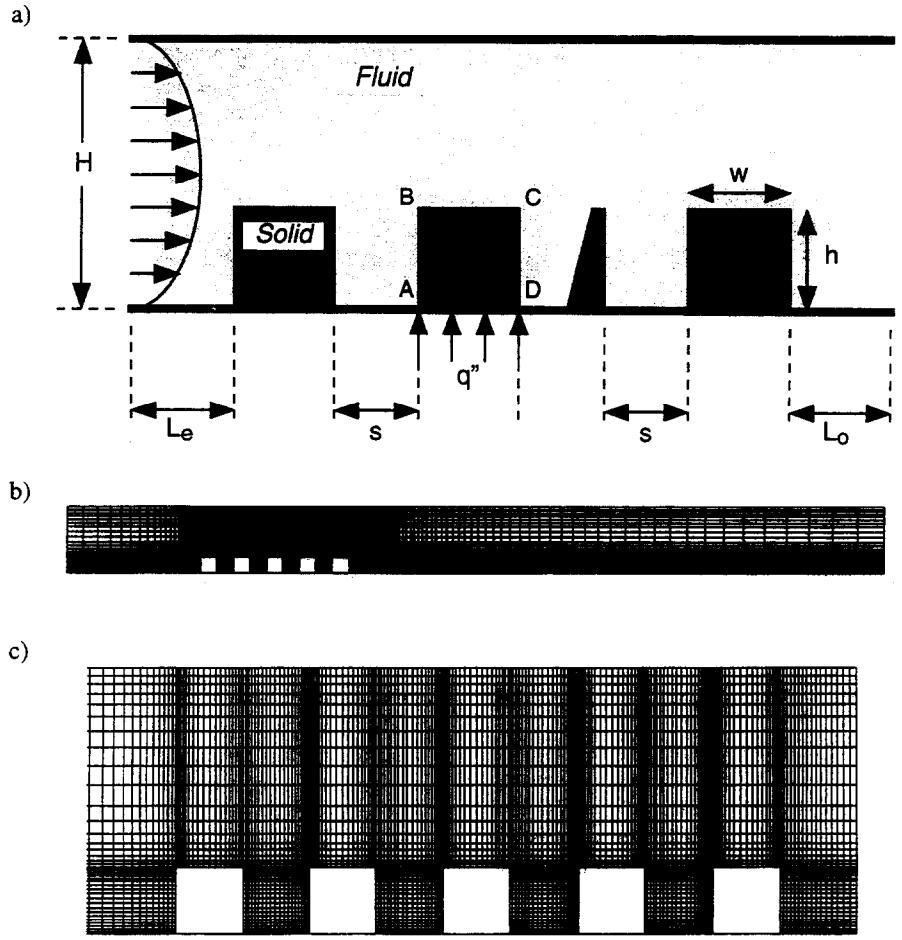

Fig. 1. (a) Schematic diagram of the multiple heat obstacle problem, (b) a typical computational domain mesh plot, and (c) a close-up of the near-obstacle region. The mesh within the obstacles is not shown for clarity.

The parameter N $(=1,2,\ldots,N_t)$ is the obstacle number and N_t is the total number of heated obstacles.

2.2. Numerical method

The solution to the governing equations was found through the Galerkin finite element method. Nine node quadrilateral elements were utilized to discretize the problem domain and the dependent variables were approximated using biquadratic interpolation functions. A residual was found for each of the governing conservation equations through substitution of the interpolation functions. In the Galerkin method these residuals are reduced to zero in a weighted sense over each element by making them orthogonal to the interpolation functions, $\int_{V^e}(\psi_i \cdot \mathbf{R}_i)\,dV^e = 0$, where ψ_i is the interpolation function, $\mathbf{R}_i$ is the residual, and V^e is the element volume. This procedure yields a system of equations for each element. The global system of equations is generated by assembling the elemental equations and imposing the continuity of primary (velocity and temperature) and secondary (flux) variables. The resultant equation is expressed as $\mathbf{K}(\mathbf{U}_1, \mathbf{U}_2, \mathbf{T})\Omega = \mathbf{F}(\mathbf{U}_1, \mathbf{U}_2, \mathbf{T})$, where $\Omega = (\mathbf{U}_1, \mathbf{U}_2, \mathbf{P}, \mathbf{T})^T$ is the column vector of unknown variables, $\mathbf{K}$, the stiffness matrix, represents the diffusion and convection of energy, $\mathbf{F}$, the force vector, incorporates the boundary conditions, and $\mathbf{U}_1$, $\mathbf{U}_2$, $\mathbf{P}$, and $\mathbf{T}$ are the nodal x- and y-components of velocity, pressure, and temperature vectors, respectively.

The pressure is eliminated from the governing equations using the consistent penalty method. The continuity equation, (1), is replaced by $\nabla \cdot \mathbf{U} = -\varepsilon p$, which allows a substitution for the pressure term in the momentum equations. The continuity equation is then interpreted as a constraint on the velocities. The value of the penalty parameter was fixed at 10^{-6}. The application of this finite element technique is well documented [9].

2.3. Solution scheme

The nonlinear momentum equations are solved iteratively whereas the energy equation is subsequently solved in a single step. A composite solution strategy, employing direct Gaussian elimination, was used to assist convergence of the velocity solution. The successive substitution technique was first utilized for four solution steps. The nonlinearities were evaluated using data from the previous iteration, $\mathbf{U}_{n+1} = \mathbf{K}^{-1}(\mathbf{U}_n)\mathbf{F}$, where n is the iteration number. The succeeding iterations employed the Newton–Raphson method with the solution linearized according to $\mathbf{U}_{n+1} = \mathbf{U}_n - \mathbf{J}^{-1}(\mathbf{U}_n)\mathbf{R}(\mathbf{U}_n)$, where $\mathbf{J}(\mathbf{U}) = \partial\mathbf{R}/\partial\mathbf{U}$ is the Jacobian matrix of the system of equations $\mathbf{R} = \mathbf{KU} - \mathbf{F}$. The iterations towards the steady state solution are concluded when the following convergence criteria are satisfied.

$$\left\| 1 - \frac{\mathbf{U}_{n-1}}{\mathbf{U}_n} \right\| \leqslant \delta_{\mathbf{U}} \quad \text{and} \quad \left\| \frac{\mathbf{R}_n}{\mathbf{R}_0} \right\| \leqslant \delta_{\mathbf{R}}. \tag{13}$$

Here $\| \ \|$ is the RMS norm summed over all the equations, $\mathbf{R}_0$ is the residual computed from the initial solution vector $\mathbf{U}_0$, and the tolerances for the solution and residual vectors, $\delta_{\mathbf{U}}$ and $\delta_{\mathbf{R}}$, respectively, were set to 10^{-8}.

Solutions, for a given geometry, proceeded in several phases. First, the Reynolds number was set to its lowest value and the velocity solution was found using the related Stokes problem as the initial guess. Solutions to the energy equation were then obtained, using the converged velocity field, for each value of obstacle thermal conductivity. The Reynolds number was then incrementally increased and the momentum equations were solved using the previous velocity solution as the initial guess, followed by solutions to the energy equation. This solution strategy provides reasonable initial guesses and results in valid solutions at each step for the desired range of Reynolds numbers.

Figures 1(b) and (c) show a typical, highly variable mesh employed for the present calculations. This mesh was designed to capture the critical features near the obstacle region and to provide sufficient mesh density, with minimal element distortion, at the obstacle surfaces. Extensive tests, involving mesh densities and gradings, were performed to confirm the grid independence of the model until further refinement showed less than a one percent difference in the results. To eliminate the influences of the entrance and outlet upon the solution near the obstacle region, as described by Vafai and Kim [8], additional tests were performed by individually increasing the lengths of the channel before and after the obstacle array. Entrance effects were found to be effectively isolated with $L_e = 2$. An outlet length of $L_o = 8$ ensured that the large downstream recirculation zone was well ahead of the outlet and that the fluid exited in a parabolic profile. The meshes employed for the various geometries ranged from 374×60 to 914×76 (x, y). Both mass and energy conservation were evaluated and found to be satisfied within 0.1% and 1.2%, respectively.

To validate the numerical scheme used in the present study, initial calculations were performed for laminar flow through a channel without an obstacle. Calculated entrance region and fully developed Nusselt numbers showed excellent agreement with the analytical solution of Cess and Shaffer [10]. Next, comparisons were made with the three obstacle study of Davalath and Bayazitoglu [2]. Those obstacles were heated volumetrically with $k_s/k_f = 10$, $h = 0.25$, and $w = s = 0.5$ in a flow of $200 \leqslant Re_{D_h} \leqslant 3000$. Temperature distributions along the obstacle walls compare well, but the local Nusselt number distributions displayed a difference. Along the left (**AB**) and right (**CD**) faces their local Nusselt number distributions do not exhibit the large increases near corners **B** and **C** that have been reported elsewhere [3, 11, 12]. Mesh coarseness neighboring the obstacle, especially near the vertical faces, appears to be the reason for the Nusselt number differences.

3. Results and discussion

The dimensionless parameters that specify this system include the hydraulic diameter ($D_h = 2H$) based Reynolds number, obstacle thermal conductivity ratio, and obstacle height, width, and spacing. In addition, the comprehensive parametric analysis included variations in heating method (surface flux versus volumetric generation), the number of obstacles in the array, and the geometrical features of obstacle size and shape. The results given in this work present only a small fraction of the cases that were investigated. The results that are shown were chosen to exemplify the pertinent features and characteristics. Further, in order to illustrate the results of the flow and temperature fields near the obstacle array only this region and its vicinity is focused upon. However, it should be noted that the computational domain included a much larger region than what is displayed.

The range of Reynolds numbers in this investigation, $200 \leqslant Re_{D_h} \leqslant 2000$, was chosen such that laminar conditions were maintained. This range of values is typical of laminar forced convective cooling of electronic systems, where the inlet velocity may range from 0.3 to 5 m s^{-1} [13]. The thermal conductivity was varied from $k_s/k_f = 10$ to 1000, values typical of materials utilized in electronic packaging, such as epoxy glass, ceramics, heat spreaders, and encapsulants.

The obstacle geometries were parametrically varied to evaluate the effects of systematic changes. Figure 2 shows a comparative sketch, relative to the unity channel spacing, of the baseline case and the sets of cases investigated, grouped by geometry. To summarize, the geometric variations are as follows: $w = 0.125$–0.5, $h = 0.125$–0.25, and

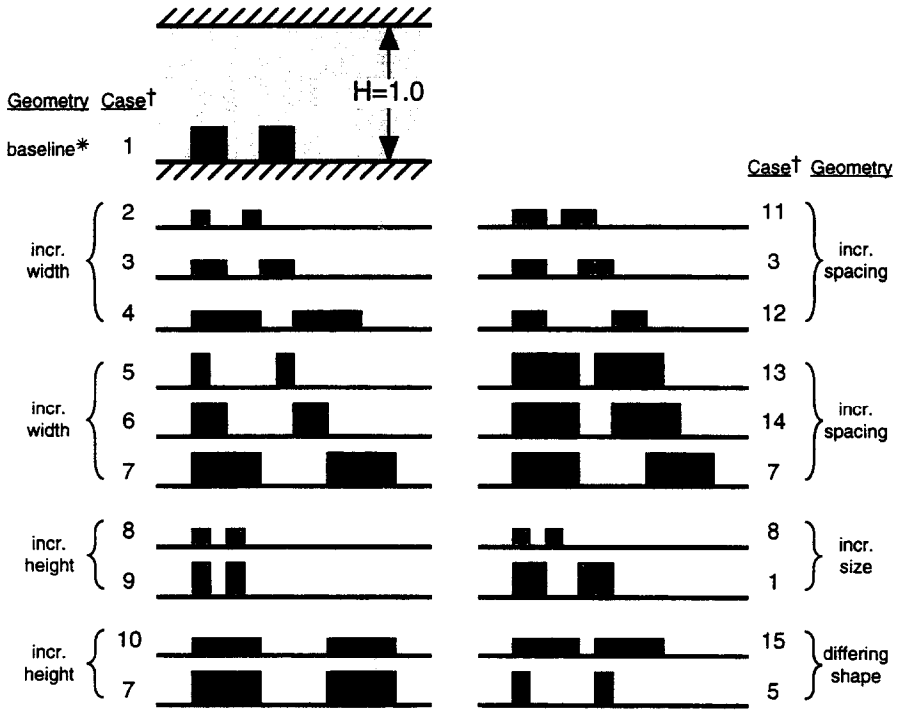

Case†	w	h	s	Case†	w	h	s	Case†	w	h	s
1*	0.25	0.25	0.25	6	0.25	0.25	0.5	11	0.25	0.125	0.125
2	0.125	0.125	0.25	7	0.5	0.25	0.5	12	0.25	0.125	0.5
3	0.25	0.125	0.25	8	0.125	0.125	0.125	13	0.5	0.25	0.125
4	0.5	0.125	0.25	9	0.125	0.25	0.125	14	0.5	0.25	0.25
5	0.125	0.25	0.5	10	0.5	0.125	0.5	15	0.5	0.125	0.125

Fig. 2. Comparative sketch of the multiple obstacle cases investigated (only two of five obstacles shown per case).

$s = 0.125$–0.5. The fixed input parameters utilized in this work are $H = 1$, $L_c = 2\text{m}$ $L_o = 8$, $q'' = 1$, and $Pr = 0.72$.

The effects upon the flow and thermal fields are illustrated through comparisons with the baseline, Case 1, of five surface flux heated obstacles with $w = 0.25$, $h = 0.25$, $s = 0.25$, $Re_{D_h} = 800$, and $k_s/k_f = 10$. Several general features were found in all the cases investigated. The presence of the upstream obstacle in the array causes the flow to turn upwards and accelerate into the bypass region (*vena contracta*). This core flow causes a very weak clockwise vortex to form forward to corner A of the first obstacle. Though the details are not shown for brevity, the vortex strength slightly increases and the triangular shaped recirculation region occupies slightly more area as Re_{D_h} increases. The velocity magnitudes within these recirculations remain two or three orders of magnitude less than that within the core flow. The core flow also produces two other vortex effects when it interacts with the obstacle array: recirculations within the interobstacle cavities and a large recirculation zone downstream of the array.

3.1. Effects of the Reynolds number

All of the vortices are affected by changes in Reynolds number. The weak strength of the upstream vortex precludes its appearance in Fig. 3, where Re_{D_h} is varied from 200 to 2000. The downstream recirculation zone (beyond the last obstacle) expands axially and gains strength as Re_{D_h} increases. The fluid core flow, through increasing viscous effects, pulls the vortex into a strong rotation and extends the vortex further downstream as the increased core flow axial momentum inhibits its expansion into the full channel. Again, it should be pointed out that the computational domain outlet was positioned far beyond the regions shown in the figures.

The production of the interobstacle vortices is similar to the classic driven cavity problem with the exception

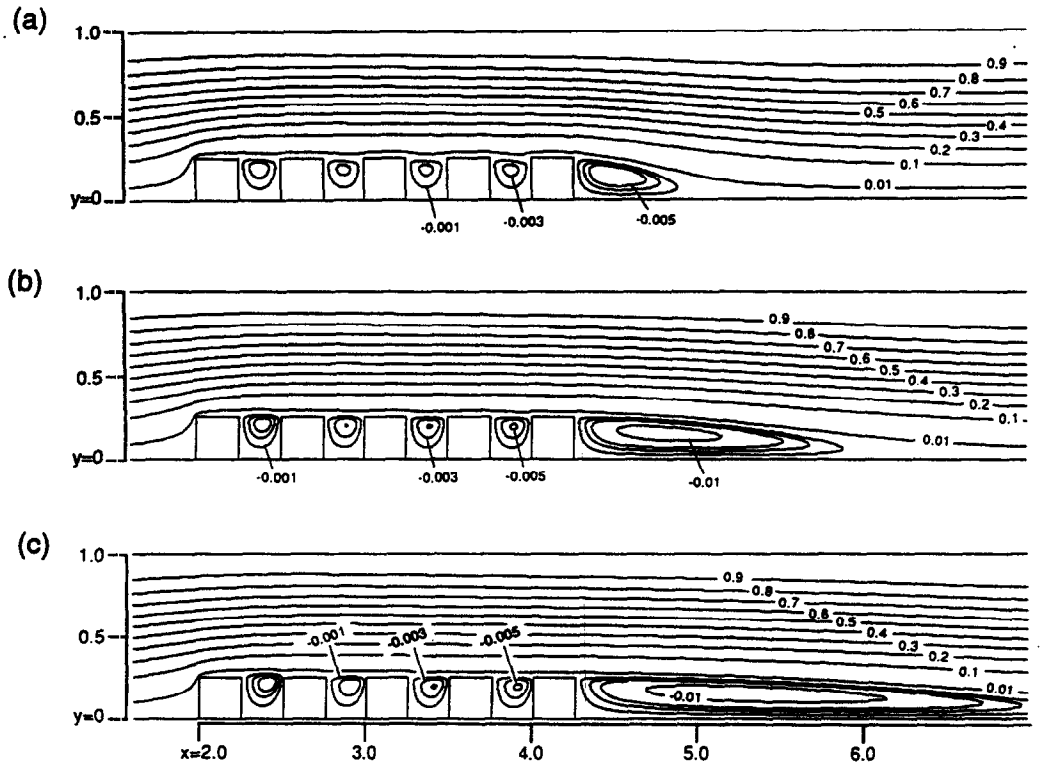

Fig. 3. Effects of the Reynolds number on streamlines for flow in a parallel plate channel for the baseline case: $w = 0.25$, $h = 0.25$, and $s = 0.25$: (a) $Re_{D_h} = 200$, (b) 800, and (c) 2000.

that the solid, moving lid is replaced by the fluid core flow. At the lowest Reynolds number, Fig. 3(a), the fluid is able to expand downward slightly towards the cavity after flowing past an obstacle. This downward pressure prevents the vortices from rising upwards past the plane of the obstacle top faces. Detailed streamline plots, not shown for brevity, show that this effect is greater at downstream cavities. At higher Reynolds numbers, the cavity vortices, especially the first, are able to rise above the obstacle top face planes due to increased circulation strength and the decreased pressure in the core flow. The increased core flow axial momentum also acts in a similar manner on the interobstacle vortices as it does on the downstream vortex: it pulls the vortex centers downstream (albeit slightly) and increases the strength of the recirculations through increased viscous shear. Downstream of the first cavity, the size, strength, and location of the vortices appear similar, suggesting possible periodicity. Further detailed discussion of periodicity is presented later with regard to the number of obstacles.

The local Nusselt number distributions around the exposed faces of the five heated obstacles, for the baseline case with $k_s/k_f = 10$, and $Re_{D_h} = 200$ to 2000, are shown in Fig. 4. Each plot shows the Nu_x distributions for the periphery of all five obstacles in the array. For the left (**AB**) and top (**BC**) faces, Nu_x always decreases for the downstream obstacles. The opposite is true for Nu_x along the right faces. The first obstacle has much larger Nu_x values along its left face than the other obstacles due to the impact of the core flow as it is redirected into the bypass region. The last obstacle in the array has the largest Nu_x values along its right face. This effect becomes more pronounced as Re_{D_h} increases because the stronger core flow produces a larger and stronger downstream recirculation which is able to convect more thermal energy away from the array. The remaining vertical surfaces within the obstacle array (both **AB** and **CD**) have lower Nu_x values because of their isolation from the core flow. The thermal transport from these surfaces is dominated by the cavity vortices. The vortices, moving clockwise, pick up thermal energy from face **AB** and transport it to the right face, **CD**, of the preceding obstacle. It should be noted that heat transfer does not occur from **CD** to **AB** due to the convective interaction between the vortex and the core flow. This upstream thermal transport heats the fluid near the upstream obstacle face **CD**, to the point where local heat transfer into the upstream obstacle, signified by the negative values of Nu_x, occurs in some cases. This is most apparent at the first cavity as the temperature difference is greatest between the second

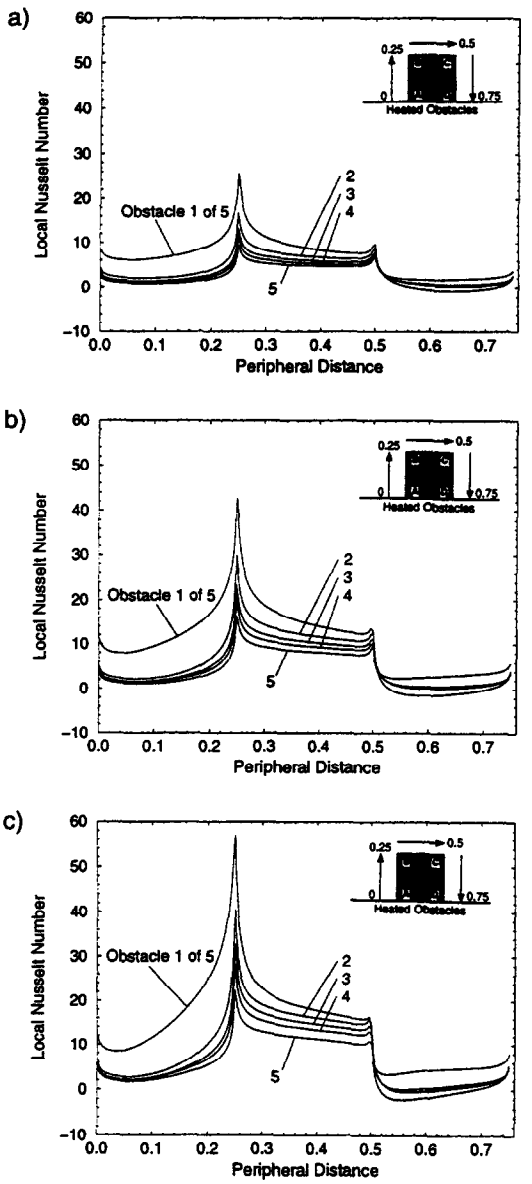

Fig. 4. Effects of the Reynolds number on local Nusselt number distributions for the baseline case with $k_s/k_f = 10$ and (a) $Re_{D_h} = 200$, (b) 800, and (c) 2000.

obstacle and the first obstacle, which is cooled considerably more at its left and top faces.

3.2. Effects of the thermal conductivity ratio

The solid thermal conductivity has a significant effect on the thermal transport within the obstacles. Figure 5 compares the isotherms at $Re_{D_h} = 800$ for the baseline case using $k_s/k_f = 10$ and 1000. As expected, increasing the thermal conductivity reduces the temperatures and thermal gradients within the obstacles by reducing the internal resistance to heat flow. When the thermal conductivity is larger than $k_s/k_f = 100$, the obstacles become essentially isothermal and the Nu_x distributions become nearly identical. The temperatures at the obstacle centers for surface flux heating are listed in the first two rows of Table 1(a). The difference in temperatures between obstacles three and four is 8–9% while between obstacles four and five it is 2% or less. If such a single temperature is used to completely characterize the thermal state of an obstacle, as frequently done in experimental studies [1, 5, 6], Nusselt numbers will appear row independent by row three to five as the variations will be within the estimated uncertainty.

The local Nusselt number distribution for the baseline with $k_s/k_f = 1000$ and $Re_{D_h} = 800$ is shown in Fig. 6(a). In comparing this result with that for $k_s/k_f = 10$, Fig. 4(b), several features are apparent. The values of Nu_x near both upper corners, **B** and **C**, is much greater for $k_s/k_f = 1000$. A two-dimensional control volume around these corners shows that the ratio of convective surface area to solid (conductive) mass is twice that of a surface point away from the corners. This apparent 'local' increase in convective surface area is able to draw more thermal energy away from the interior and regions with lower heat transfer rates because of the reduced internal thermal resistance. The local Nusselt numbers are slightly less along the top face **BC** when k_s/k_f is larger, especially for the first obstacle in the array where Nu_x has its largest local value. Along the left faces (**AB**), Nu_x is larger for obstacle 1, with smaller increases for the downstream obstacles, when the thermal conductivity is larger. Along the right faces (**CD**), when $k_s/k_f = 1000$, Nu_x is slightly greater near upper corner **C** but decreases to nearly constant values less than that found for $k_s/k_f = 10$. There is also no local rise in Nu_x at the bottom corner **D** when k_s/k_f is large. These effects are due to the excellent internal thermal energy transfer when $k_s/k_f = 1000$.

The temperatures along the exposed obstacle surfaces for the baseline case, with $Re_{D_h} = 800$ and $k_s/k_f = 10$ and 1000, are shown in Fig. 6(b). The obstacle surfaces are nearly isothermal when $k_s/k_f = 1000$, with the surface temperatures of the last two obstacles in the array nearly identical. The wall temperatures for $k_s/k_f = 1000$ are lower than for $k_s/k_f = 10$, except near corners **B** and **C**. When $k_s/k_f = 10$, increased conduction resistance results in temperature gradients between **AD**, the heat input site, and the top face **BC**, where Nu_x is greatest. Upper corners **B** and **C**, where the convective transport is greatest, have lower temperatures when $k_s/k_f = 10$ because increased conduction resistance inhibits thermal energy flow to maintain higher temperatures. As one moves towards the heated region (**AD**), the surface temperatures are seen to increase as the increased conduction resistance inhibits thermal energy transport away to other regions of the solid with greater convection rates.

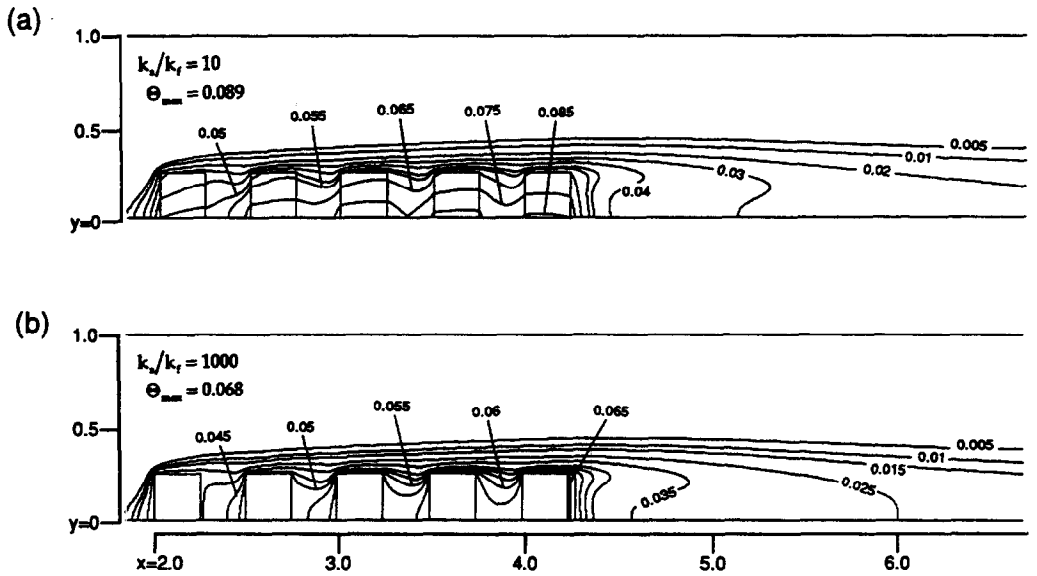

Fig. 5. Effects of the solid thermal conductivity ratio on isotherms for the baseline case using $Re_{D_h} = 800$ and (a) $k_s/k_f = 10$ and (b) 1000.

Table 1
Nondimensional temperatures ($\times 10^2$) at the obstacle centers with $w = 0.25$, $h = 0.25$, $s = 0.25$, $Re_{D_h} = 800$, and $k_s/k_f = 10$ and 1000: (a) for the five obstacle array with various heat input methods and (b) for the ten obstacle array

(a)

Heating method	k_s/k_f	Obstacle 1	Obstacle 2	Obstacle 3	Obstacle 4	Obstacle 5
Surface	10	4.248	6.193	7.132	7.715	7.571
Surface	1000	3.367	5.258	6.183	6.781	6.795
Volumetric	10	4.001	5.949	6.884	7.472	7.376
Volumetic	1000	3.365	5.255	6.180	6.778	6.793

(b)

Obstacle	$k_s/k_f = 10$	$k_s/k_f = 1000$
1	4.249	3.368
2	6.198	5.263
3	7.156	6.206
4	7.850	6.899
5	8.438	7.488
6	8.961	8.012
7	9.433	8.483
8	9.847	8.899
9	10.13	9.201
10	9.752	8.980

3.3. *Effects of the heat input method*

The two different methods generally utilized to approximate the thermal energy release in electronic components are an input surface flux at the obstacle base (**AD**) and uniform volumetric energy generation. Utilizing the velocity fields found for the baseline case, solutions to the energy equations, (5), with $\vartheta = 1$ and no heat flux at **AD**, were found. Figures 7(a) and (b) show the isotherms near the obstacle region with $Re^*_{D_h} = 800$ and

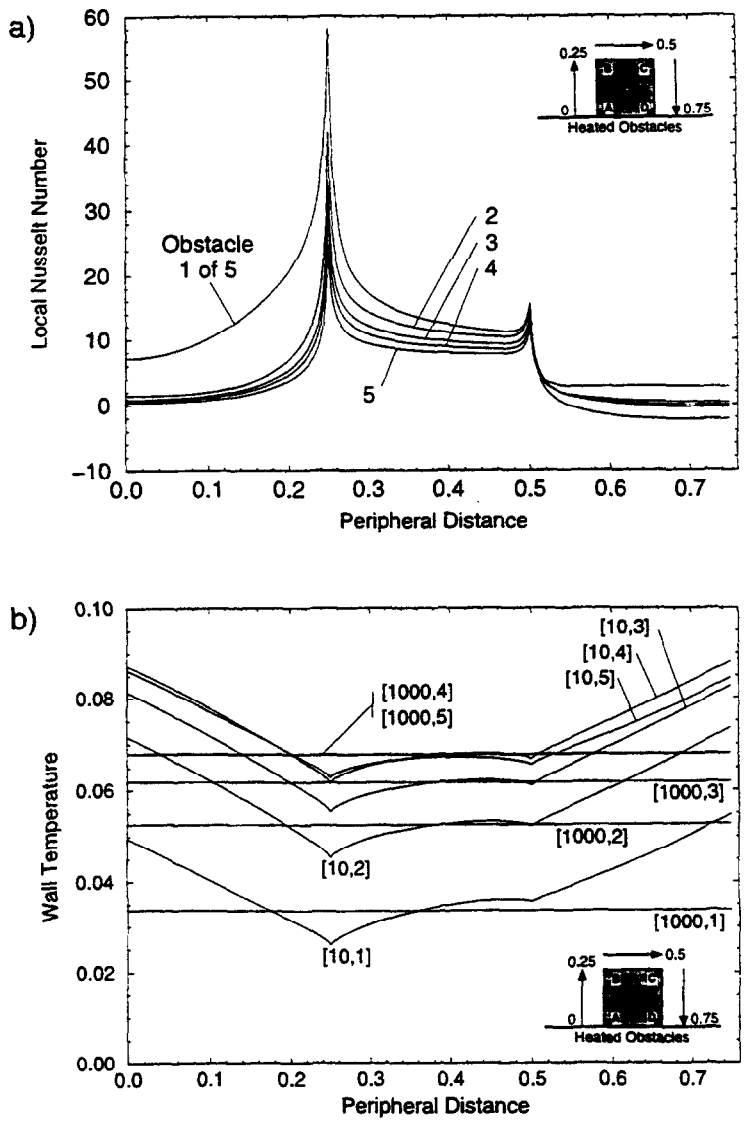

Fig. 6. (a) Local Nusselt number distributions for the baseline case with $k_s/k_f = 1000$ and (b) comparison of wall temperatures for the baseline case with $k_s/k_f = 10$ and 1000, all at $Re_{D_h} = 800$. Key: [k_s/k_f, obstacle number].

$k_s/k_f = 10$ and 1000, respectively. Several differences can be seen compared with the isotherms of Fig. 5 where the obstacles were surface flux heated. For $k_s/k_f = 10$ the maximum temperature, found in the fourth obstacle, is less for volumetric heating and its position is more centrally located within the obstacle. This is due to the energy generation, by definition, being well distributed throughout the obstacle volume versus a surface flux along one face. When $k_s/k_f = 1000$, however, differences between the isotherms for the two heating cases are very small and the maximum temperatures obtained are identical. Table 1(a) documents the obstacle center temperatures, showing the 6% or less decrease for volumetric heating when $k_s/k_f = 10$ and almost identical temperatures when $k_s/k_f = 1000$. Very little variation in $\overline{Nu}_m$ is observed at an individual obstacle, for either heating method or thermal conductivity, consistent with an energy balance around an obstacle. Comparisons between the known heat input rate, $q_m = \int q'' \, dA$ or $\int q''' \, dV$, compare extremely well with the thermal energy leaving the obstacle and entering the fluid, calculated from $q_{out} = \int Nu_x(x)\Theta_w(x) \, dA$.

3.4. Effects of the number of obstacles in the array

To investigate whether the Nusselt numbers become periodic within the array, the baseline case was extended

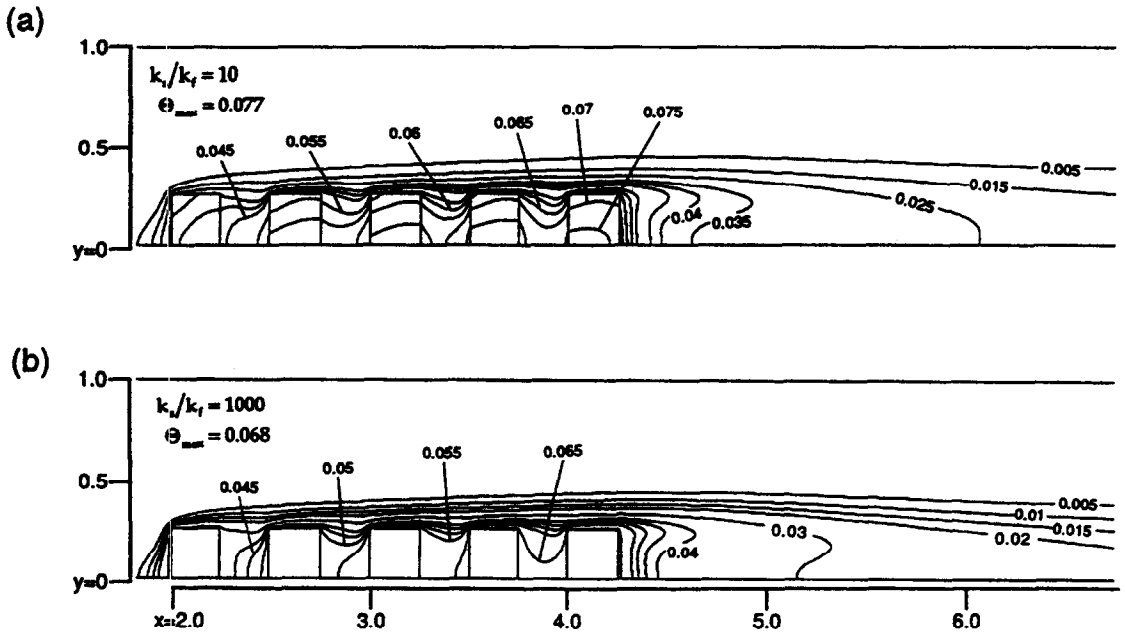

Fig. 7. Temperature contours for the baseline case with volumetric heat generation within the obstacles for $Re_{D_h} = 800$, (a) $k_s/k_f = 10$, and (b) $k_s/k_f = 1000$.

to ten identical, heated obstacles with dimensions $w = 0.25$, $h = 0.25$, and $s = 0.25$. The velocity fields were then calculated for $200 \leqslant Re_{D_h} \leqslant 2000$ and thermal solutions were found for $k_s/k_f = 10$ and 1000.

Figure 8 gives the results for overall and exposed surface mean Nusselt numbers for the ten individual obstacles with $k_s/k_f = 10$. The overall, left, and top mean Nusselt numbers show the greatest changes between the first and second obstacle with a smaller change between the last obstacles in the array. The reverse effect occurs for the right side Nusselt number, $\overline{Nu}_R$, as the large downstream vortex has a stronger effect upon the heat transfer, compared with the cavity vortices, along the right faces (**CD**). Using obstacle nine as the reference to avoid the end of array effects found at the last obstacle, the value of $\overline{Nu}_M$ for obstacle eight differs only by about 5% for both $Re_{D_h} = 200$ and $Re_{D_h} = 2000$. A 10% difference in $\overline{Nu}_M$ was found between the seventh and ninth obstacles. Due to the interrupted boundary layer development, the top face mean Nusselt numbers show the most reluctance in achieving row independent values (a 5% difference between $\overline{Nu}_T$ for the eight and ninth obstacles). This effect manifests itself in the values of $\overline{Nu}_M$ not achieving the expected fully developed values early on in the array. The five percent criterion was found to be too stringent for the left face mean Nusselt number, with $\overline{Nu}_L$ for obstacle eight differing from that at the ninth by 10%. For the right face mean Nusselt number, using the eighth obstacle as the reference, the values of $\overline{Nu}_R$ at the fourth through seventh obstacle are within about 5%.

A further assessment of the periodicity within the array was made by observing the values of the three degrees of freedom (u, v, Θ) at boundary **E′C′D′** of 'unit cell' **DCEE′C′D′** (Fig. 9). Periodic boundary conditions are frequently employed to reduce computational domains. The explicit requirement is that, after an initial entry region, the flow patterns repeat periodically. The large numbers of obstacles in this array allowed the evaluation of periodic boundary conditions for forced convective flows in channels with heated, discrete obstacles.

Figures 9(a) and (b) show plots of the two velocity components, with $Re_{D_h} = 800$, along the 'periodic' boundary **E′C′D′** located behind each obstacle. The values of the x-component of velocity, even at the tenth obstacle, are short of the theoretical maximum value of 2.0 for flow in a channel with no obstacles and the same height. This indicates that the bypass flow is not fully developed, due to the perturbation in the bypass channel caused by the cavities. The maximum difference between $u(y)$ at the third and tenth obstacles is 5%, with smaller differences for downstream obstacles. Away from the array entrance and exit the y-velocity components have a general 's-like' shape and fluctuate between $-0.015 < v < 0$. The values for $v(y)$ are small, only about 0.5% of y_{max}, and negative as the fluid turns to expand into the cavities. The differences in the $v(y)$ profiles behind the obstacles does not have a significant effect on the Nusselt number and the x-component of th flow field, $u(y)$.

The temperature distribution along the ten 'periodic'

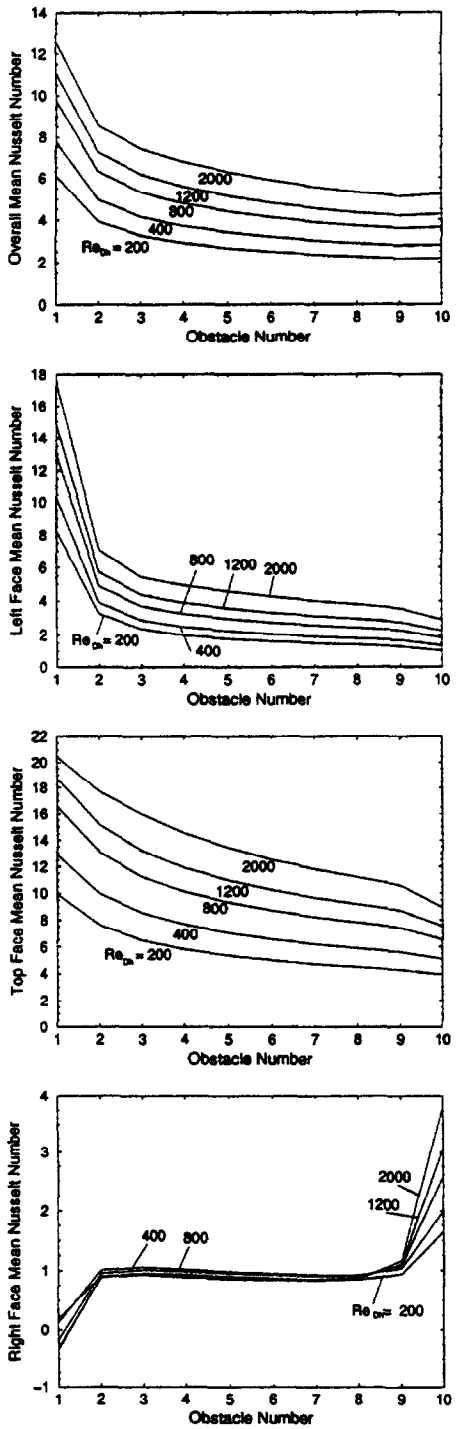

Fig. 8. Mean Nusselt numbers for the individual obstacles in a ten obstacle array with $w = 0.25$, $h = 0.25$, $s = 0.25$, $k_s/k_f = 10$, and $200 \leqslant Re_{D_h} \leqslant 2000$.

boundaries **E′C′D′** is shown in Fig. 9(c) for $k_s/k_f = 10$. Within each 'unit cell' an equal amount of thermal energy, $q'' \times w$, is released into the system. An energy balance on a 'unit cell' yields $\Theta_m|_{E'C'D'} - \Theta_m|_{ECD} = q''w/Pe_H$, which is constant, where Θ_m is the mean temperature at a 'periodic' boundary. A plot [Fig. 9(c)-inset] of the mean fluid temperatures, $\Theta_m|_{E'C'D'} = \int_h^H \Theta_f(x, y)\,dy$, at the ten 'periodic' boundaries **E′C′D′** (away from the array entrance and exit regions) shows a linear increase. This agrees with the description of periodic temperature conditions for thermally active regions by Kelkar and Choudhury [14], who decompose the bulk temperature into a linear variation due to the thermal energy release in each repeating cell and a periodic part identical in all cells. This linear increase in temperatures is also seen in the obstacle center temperatures (except for the last obstacle as explained earlier), detailed in Table 1(b), for the ten obstacle array with $k_s/k_f = 10$ and 1000. A slight increase, less than 2%, in center temperatures was found for the first four obstacles when the ten obstacle case is compared with the data for five obstacles [Table 1(a)]. This effect is attributable to the thermal convection from the warmer upstream obstacles by the clockwise cavity vortices. The ten obstacle array, adding twice as much thermal energy into the channel compared with the five obstacle array, allows the warmer, downstream obstacles to have a greater influence on the upstream obstacles.

To recapitulate, the periodicity within the ten obstacle array has been shown at the 5% difference level and at the less restrictive 10% level. The mean Nusselt number, which reflects both fluid and thermal conditions, for obstacles eight and seven were within 5% and 10%, respectively, of the value found at obstacle nine. The local values of the velocity components and temperature at the 'periodic' boundaries clarify and support the use of periodic boundary conditions for obstacles assumed located away from the entrance. Comparisons with experimental work shows similar results. Lehmann and Pembroke [5] reported $\overline{Nu}_m$ being constant, within experimental uncertainty, for rows six to ten. Garimella and Eibeck [15] reported h_c asymptotic by the fourth row in their experiments, while Souza Mendes and Santos [16] had independent Sherwood numbers after row five in their experimental array. Jubran *et al.* [6], though, describe $\overline{Nu}_m$ as being row independent downstream of row three.

3.5. *Effects of the obstacle geometry*

The geometries of the different obstacle arrays investigated, as detailed in Fig. 2, can be organized into five groups based upon obstacle width, height, spacing, size, and shape. The effect that this geometric ordering has upon the heat transfer will be gauged through the mean Nusselt numbers defined by equation (8). The four areas

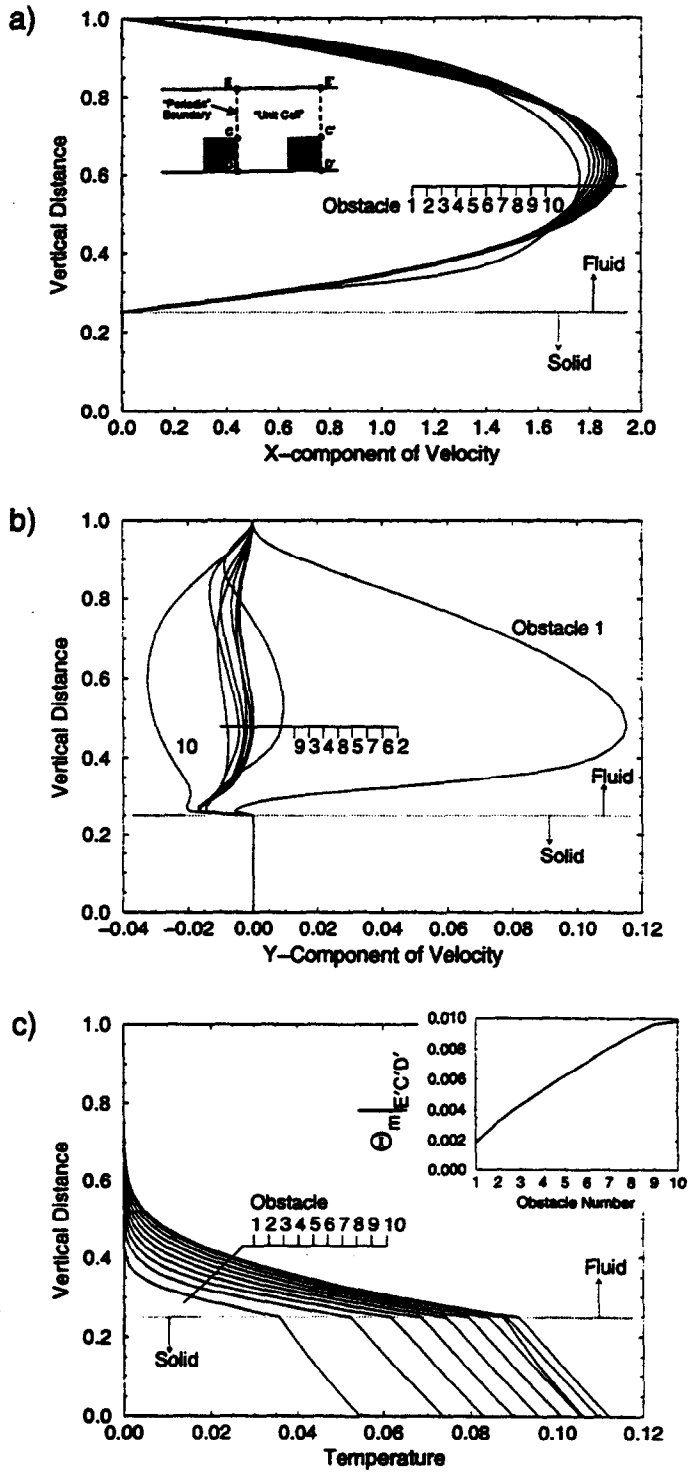

Fig. 9. The (a) x-velocity component, (b) y-velocity component, and (c) temperature at the 'periodic' boundaries **E′C′D′** of the 'unit cells' for a ten obstacle array: $w = 0.25$, $h = 0.25$, $s = 0.25$, $k_s/k_f = 10$, and $Re_{D_h} = 800$.

of interest will be left (**AB**), top (**BC**), and right (**CD**) exposed faces and the total exposed surface area of the obstacles. For these comparisons, the thermal conductivity ratio was fixed at $k_s/k_f = 1000$ and the Reynolds number was varied between 200 to 2000.

3.6. Obstacle width

The effects of varying the obstacle width from 0.125 to 0.5 is shown in Fig. 10. Here, comparisons are made between (a) Cases 2, 3, and 4 ($h = 0.125$, $s = 0.25$) and (b) Cases 5, 6, and 7 ($h = 0.25$, $s = 0.5$). In Fig. 10(a) it is seen that the narrowest obstacles of Case 2 have the highest values of $\overline{Nu}_m$, with decreasing values as the width increases. This is a direct result of $\overline{Nu}_T$ decreasing with increasing width, due to a larger percentage of the top face having lower Nu_x values because of increased distance from corner **B**. It was also found that, as expected, the first obstacles have much larger $\overline{Nu}_L$ values and the last obstacles have larger values of $\overline{Nu}_R$. In Fig. 10(a), for obstacle numbers 2 to 5, increases in width produce small differences in $\overline{Nu}_L$ as indicated by the relative clustering of the $\overline{Nu}_L(Re_{D_h})$ plots. For these obstacles, $\overline{Nu}_L$ yields little influence upon geometrical changes in $\overline{Nu}_m$. The values of $\overline{Nu}_R$ also decrease with increased width, but their small magnitudes produce small effects on the overall heat transfer. This decrease is due to the larger amount of thermal energy released by the wider obstacles further heating the fluid and reducing the heat transfer.

The results for the mean Nusselt numbers of Cases 5, 6, and 7 are found in Fig. 10(b). The plots of $\overline{Nu}_m$ are more closely clustered by obstacle number than for the similar comparison between Cases 2, 3, and 4. The values of $\overline{Nu}_L$ behave similar to those in Fig. 10(a) while $\overline{Nu}_R$ shows clusterings by the case number, except for the first and last obstacles (1 and 5) which have similar values for all three cases. As in the previous case [Fig. 10(a)], $\overline{Nu}_T$ decreases with an increase in width even though this decrease is less pronounced than the previous case. The decrease in Nusselt numbers from Cases 2, 3, and 4 [Fig. 10(a)] and Cases 5, 6, and 7 [Fig. 10(b)] are explained in the following section regarding obstacle height.

3.7. Obstacle height

Cases 8 and 9 ($w = s = 0.125$) are compared in Fig. 11(a) to present the changes in mean Nusselt numbers as the obstacle height increases from 0.125 to 0.25. The shorter obstacles have considerably larger values of $\overline{Nu}_m$. Along the top faces, except for the first obstacles, the values of $\overline{Nu}_T$ for the two different geometries [Figs. 11(a) and 11(b)] are similar, with the taller obstacles having slightly larger values. Though the core flow velocity increases as the bypass region is made smaller, values of $\overline{Nu}_T$ for the taller first obstacle are smaller than that for the shorter obstacles and increases relatively slightly as the flow rate increases beyond $Re_{D_h} \geqslant 1200$. With the greater obstacle height, the core flow is further accelerated into the bypass. Due to the incipient formation of a separation bubble along the top face of the first obstacle, which can be clearly seen at higher Reynolds number simulations, this region has a lower local velocity and decreased Nusselt number. Along the right face of the first obstacle of Case 8, [8, 1], and the first two obstacles of Case 9, [9, 1] and [9, 2], negative values of $\overline{Nu}_R$ are seen. Though in all cases the cavity vortices are weak, the greater cavity height to width ratio ($h/w = 2$) in Case 9 reduces the interaction and mixing of the vortices with the core flow. This allows the vortices in the first two cavities to transfer heat upstream into the first two obstacles. Case 8, with a smaller cavity aspect ratio ($h/w = 1$), only has negative $\overline{Nu}_R$ values at the first obstacle.

The effects of obstacle height are also shown in Fig. 11(b) where Case 10 is compared with Case 7 (both $w = s = 0.5$). The shorter obstacles have larger values of $\overline{Nu}_m$. This results from greater Nusselt numbers along the vertical faces and comparable $\overline{Nu}_T$ values. In general, the shorter cavity height does allow better thermal transport out of the cavities and into the cooler core flow. The taller obstacles, as in Fig. 11(a), have larger Nusselt numbers along the top face except, again, for the first obstacle at larger Re_{D_h}. The Nusselt numbers along the right faces are considerably different for these two cases, except that $\overline{Nu}_R$ at the last obstacles increases in both cases with the flow rate. For the shorter obstacles of Case 10, $\overline{Nu}_R$ decreases downstream whereas the reverse is true for Case 7. The interior obstacles (2, 3, and 4), for Case 7, have very comparable $\overline{Nu}_R$ values, indicating that the flow development and interaction at the second through fourth cavities is similar. The first obstacle has small and nearly constant values of $\overline{Nu}_R$ (with respect to changes in Reynolds number) because the core flow is accelerating into the bypass, reducing its interaction with the first cavity. At the last obstacle, $\overline{Nu}_R$ keeps increasing with flow rate as the thermal transport due to the downstream recirculation increases.

3.8. Obstacle spacing

The effects of increasing the obstacle spacing in the arrays from 0.125 to 0.5 is shown in Fig. 12(a) for Cases 11, 3, and 12 ($w = 0.25$, $h = 0.125$). The wider spaced array has the largest mean Nusselt numbers for virtually all faces of all obstacles. The values along the left face, save for that of the first obstacle, which is affected only by the forward recirculation and the impingement of the core flow, show that the wider spacing allows the core flow to further mix with the fluid in the cavities. This increases the transfer of thermal energy out from the cavities and into the core flow, reducing the transport towards the upstream obstacles. Along the top faces the

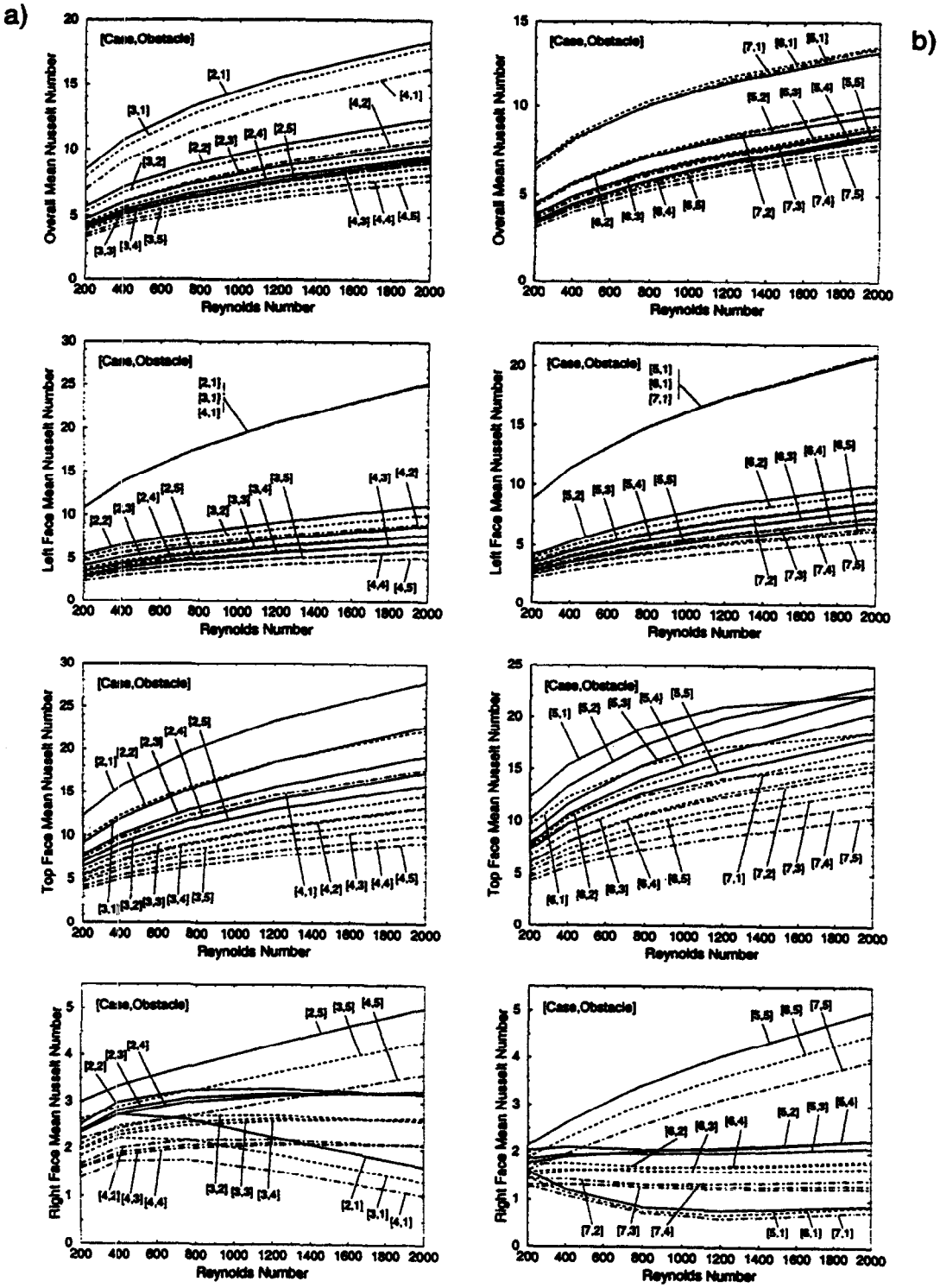

Fig. 10. Effects of obstacle width on the mean Nusselt numbers with $k_s/k_f = 1000$ and $200 \leqslant Re_{D_h} \leqslant 2000$, for (a) Cases 2, 3, and 4 and (b) Cases 5, 6, and 7. Key: [case number, obstacle number].

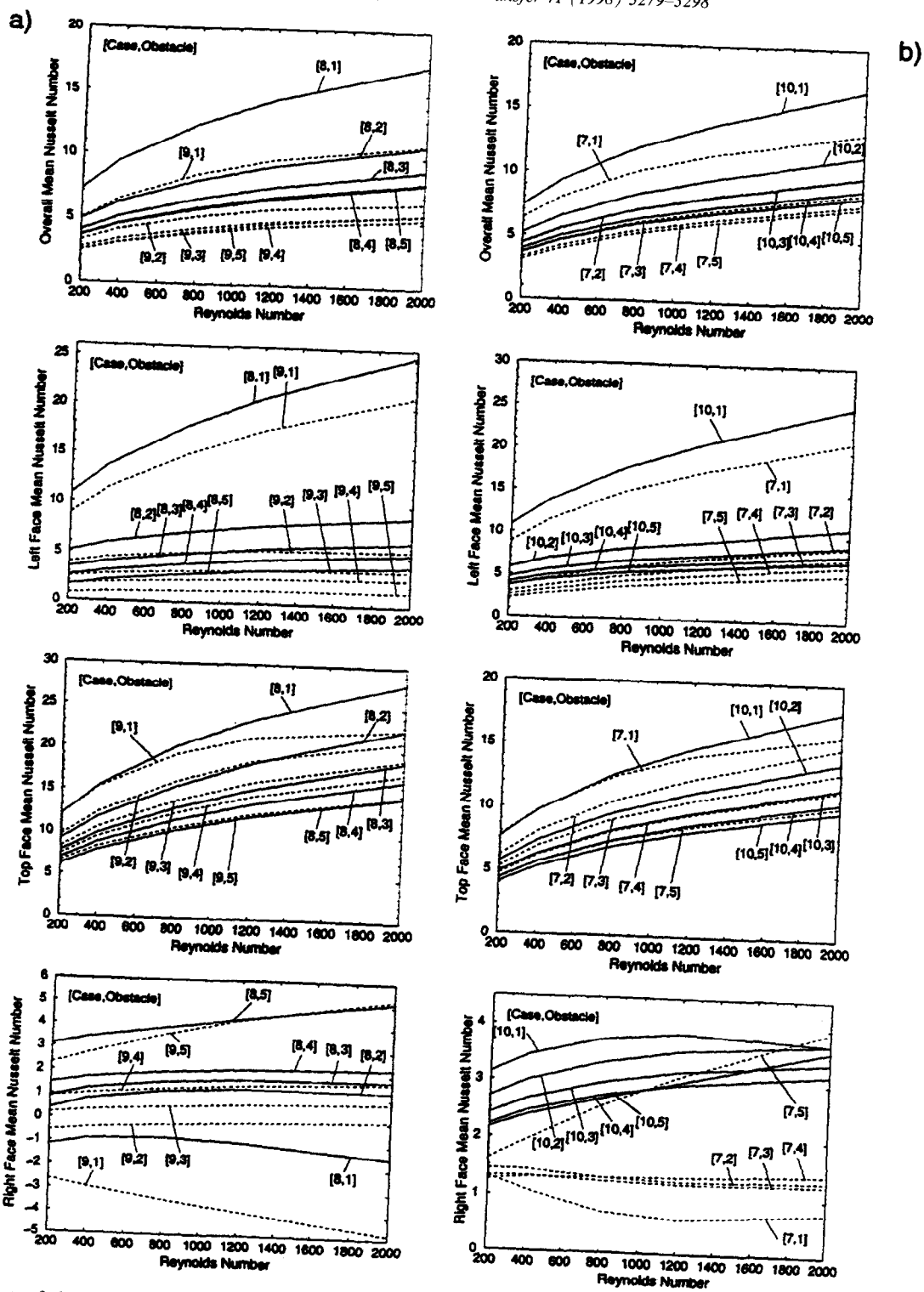

Fig. 11. Effects of obstacle height on the mean Nusselt numbers, with $k_s/k_f = 1000$ and $200 \leqslant Re_{D_h} \leqslant 2000$, for (a) Cases 8 and 9 and (b) Cases 10 and 7. Key: [case number, obstacle number].

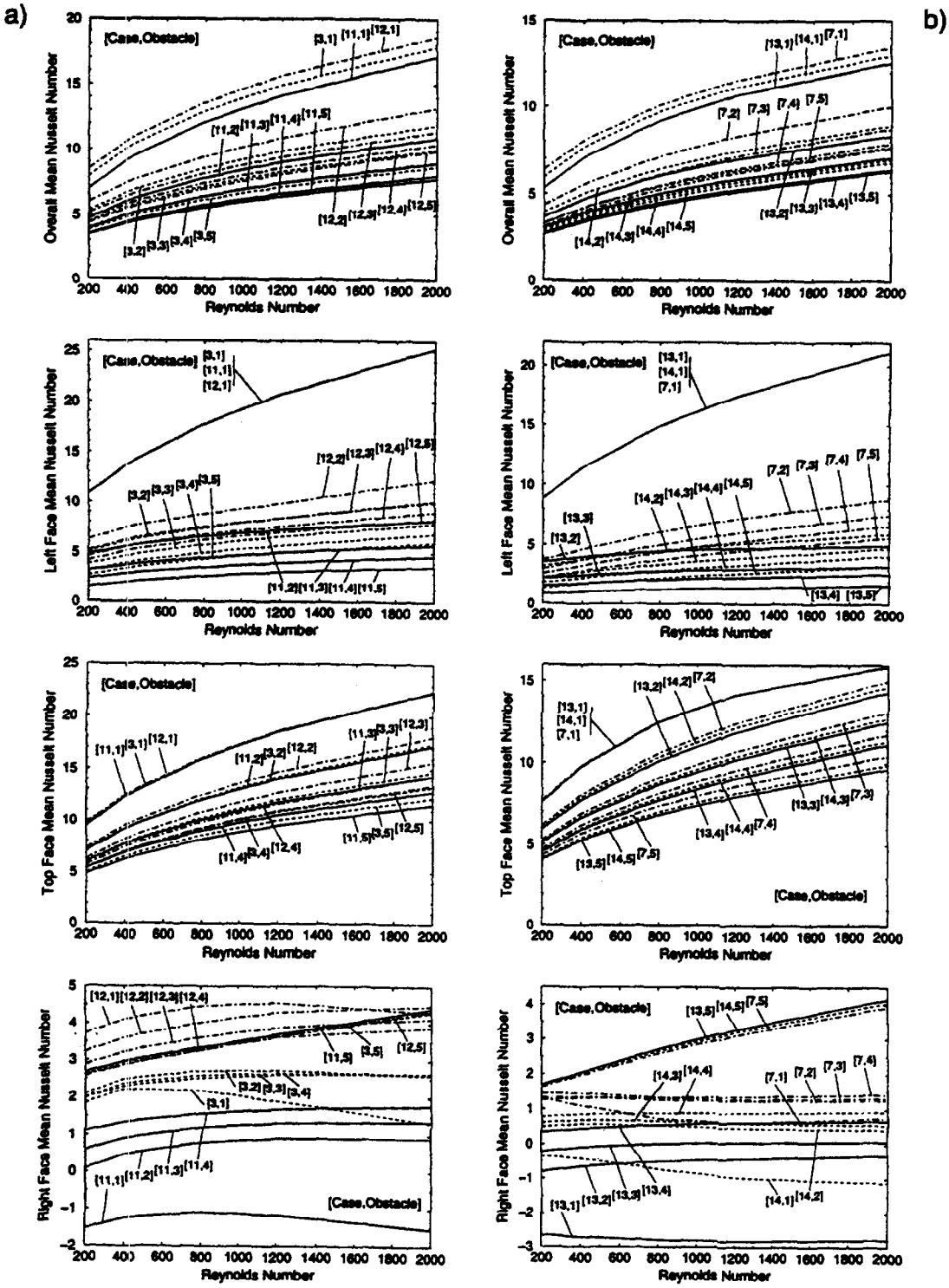

Fig. 12. Effects of obstacle spacing on the mean Nusselt numbers with $k_s/k_f = 1000$ and $200 \leqslant Re_{D_h} \leqslant 2000$, for (a) Cases 11, 3, and 12 and (b) Cases 13, 14, and 7. Key: [case number, obstacle number].

wider spaced obstacles have only a slight advantage in $\overline{Nu}_T$. The graph of $\overline{Nu}_R$ clearly shows that as the spacing is reduced the thermal transport is impeded. Similar results are also seen in Fig. 12(b) for Cases 13, 14, and 7, where $w = 0.5$ and $h = 0.25$.

3.9. Obstacle size

Case 8 ($w = h = s = 0.125$) and Case 1 ($w = h = s = 0.25$) were compared to investigate the effects of an increase in obstacle size. The obstacle volume for Case 1 is greater, even though the aspect ratio for both cases is $w/h = 1$. As shown in Fig. 13, all of the mean Nusselt numbers decreased with increased obstacle size. The smaller obstacles introduce less thermal energy into the fluid, due to their smaller width along the surface (**AD**) receiving the heat flux, reducing the obstacle wall temperatures and the thermal boundary layer penetration into the fluid. The fluid remains cooler and is thus able to transport more thermal energy away from the obstacles, as indicated by the greater Nusselt numbers. The larger obstacle height of Case 1 also increases the cavity height, further reducing the Nusselt numbers along the vertical faces and $\overline{Nu}_T$ along the top face of the first obstacle, as detailed in previous sections.

3.10. Obstacle shape

A large difference in array geometry is found between the wide-low-closely spaced obstacles of Case 15 ($w = 0.5$, $h = s = 0.125$) and the slender-tall-widely spaced obstacles of Case 5 ($w = 0.125$, $h = 0.25$, $s = 0.5$). Along the left face, as shown in Fig. 14, the Nusselt numbers are greater for Case 5, other than for the first obstacle, as the wider spacing allows better thermal transport out of the cavity. The shorter first obstacle of Case 15, however, has higher $\overline{Nu}_L$ values as the forward recirculation region is smaller, decreasing the left face area where the values of $\overline{Nu}_x$ are near minimum. The taller obstacles have larger values of $\overline{Nu}_T$ due to their narrower width and, to a lesser extent, the increased fluid velocity. Along the right face the shorter, closer spaced first obstacle has negative $\overline{Nu}_R$ values, indicating upstream thermal transport, while the wider spaced obstacles, with better core flow-cavity mixing, have greater corresponding Nusselt numbers.

4. Conclusions

A comprehensive numerical investigation of the fluid and thermal transport within a two-dimensional channel containing large arrays of heated obstacles is presented in this work. To the best of the authors' knowledge, it is the first time that an extensive analysis has been performed for a large array of simulated electronic com-

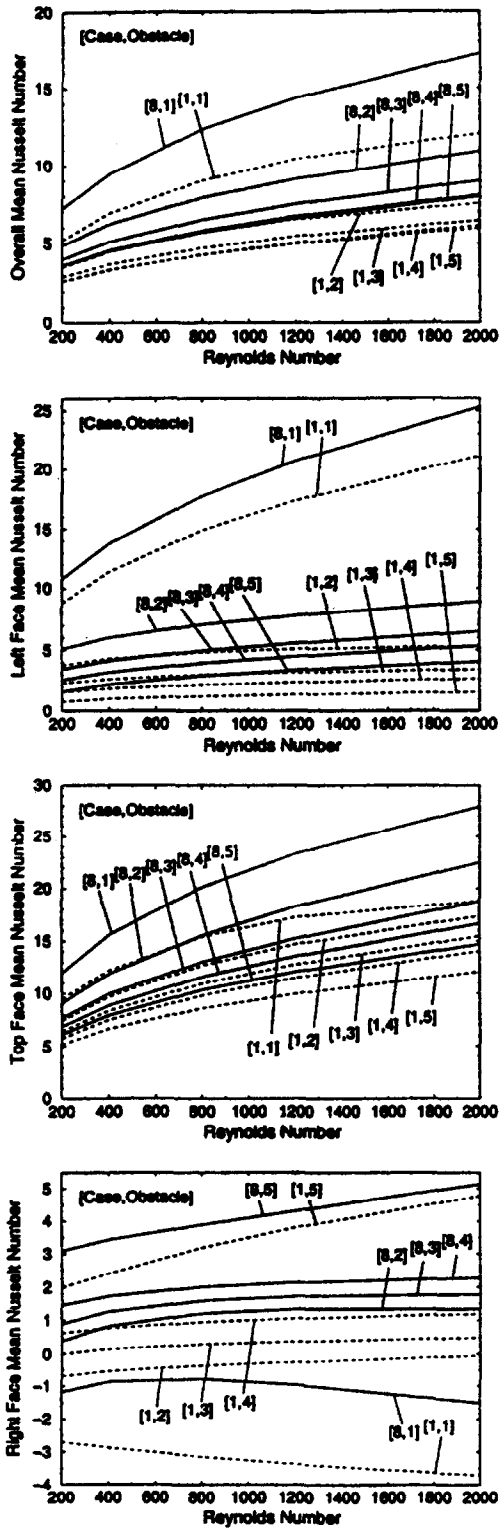

Fig. 13. Effects of obstacle size on the mean Nusselt numbers, with $k_s/k_f = 1000$ and $200 \leqslant Re_{D_h} \leqslant 2000$, for Cases 8 and 1. Key: [case number, obstacle number].

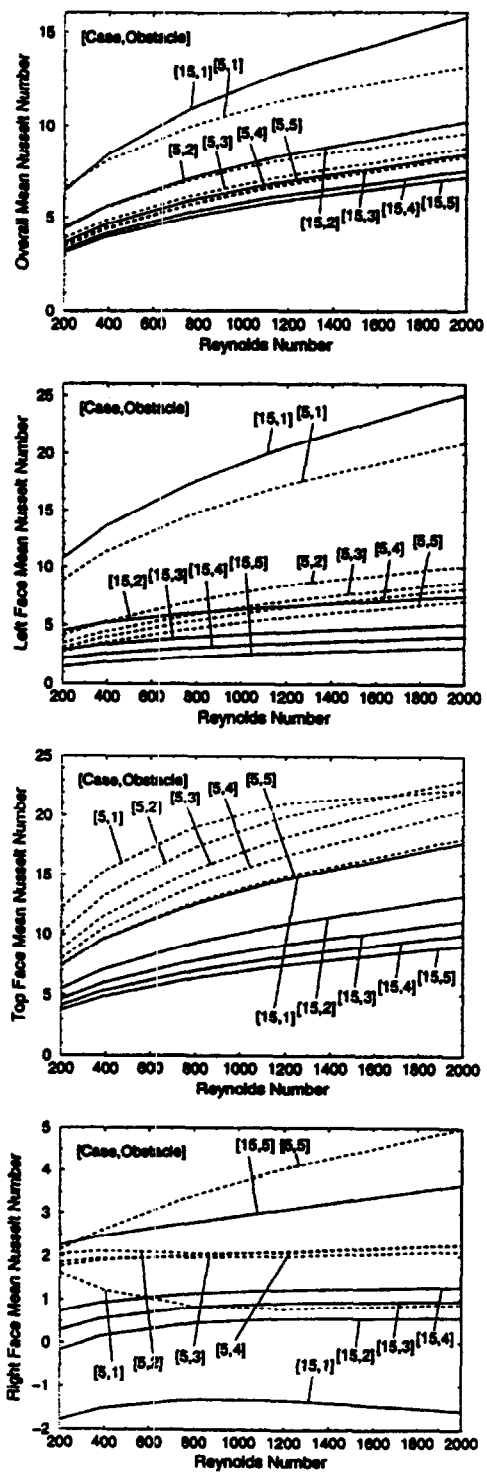

Fig. 14. Effects of obstacle shape and array geometry on the mean Nusselt numbers, with $k_s/k_f = 1000$ and $200 \leqslant Re_{D_h} \leqslant 2000$, for Cases 15 and 5. Key: [case number, obstacle number].

ponents to evaluate the fundamental results due to changes in obstacle width, height, spacing, heating method, and number. The solid thermal conductivity was varied between values typical of electronic component materials. Smaller, widely spaced obstacles were found to more effectively transfer thermal energy into the fluid, reducing their temperatures. Narrow gaps between tall obstacles were found to allow upstream thermal transport by the cavity vortices through reduced cavity–core flow interaction, in some cases actually heating the upstream obstacles. Differences between surface flux and volumetric heating manifest themselves in the isotherms within the obstacles with only small changes in Nusselt numbers. Large values of the solid thermal conductivity effectively isothermalize the obstacles regardless of heating method or geometry. Periodicity was explicitly demonstrated by doubling the number of obstacles and evaluating the mean Nusselt numbers and the calculated variables at 'periodic' boundaries between the obstacles in the array. The mean Nusselt number was found to reach the 5% and 10% difference levels, referenced to the ninth obstacle, at the eighth and seventh obstacles, respectively. Extensive presentation and evaluation of the mean Nusselt numbers along the exposed faces of all obstacles in the array was fully documented.

Acknowledgements

The support by the Aerospace Power Division of the USAF Wright Laboratory under Contract F3360196MT565 is acknowledged and appreciated. The authors acknowledge Dr Jerry Beam, Deputy for Technology, for his support on this project.

References

[1] Peterson GP, Ortega A. Thermal control of electronic equipment and devices. In: Hartnett JP and Irvine TF editors Advances in Heat Transfer, Vol. 20. San Diego: Academic Press, 1990, p. 181–314.

[2] Davalath J, Bayaszitoglu Y. Forced convection cooling across rectangular blocks. J Heat Transfer 1987;109:321–8.

[3] Kim SY, Sung HJ, Hyun JM. Mixed convection from multiple-layered boards with cross-streamwise periodic boundary conditions. Int J Heat Mass Transfer 1992;35:2941–52.

[4] Kim WT, Boehm RF. Laminar buoyancy-enhanced convection flows on repeated blocks with asymmetric heating. Numerical Heat Transfer: Part A 1992;22:421–34.

[5] Lehmann GL, Pembroke J. Forced convection air cooling of simulated low profile electronic components: Part 1—Base case. J Electronic Packaging 1991;113:21–6.

[6] Jubran BA, Swiety SA, Hamdan MA. Convective heat

transfer and pressure drop characteristics of various array configurations to simulate the cooling of electronic modules. Int J Heat Mass Transfer 1996;39:3519–29.

[7] Huang PC, Vafai K. Analysis of forced convection enhancement in a channel using porous blocks. J Thermophysics and Heat Transfer 1994;8:249–59.

[8] Vafai K, Kim SJ. Analysis of surface enhancement by a porous substrate. J Heat Transfer 1990;112:700–5.

[9] FIDAP, Theory Manual, Fluid Dynamics International, Evanston, IL, 1993.

[10] Cess RD, Shaffer EC. Heat transfer to laminar flow between parallel plates with a prescribed wall heat flux. Applied Scientific Research 1959;A8:339–44.

[11] Kang BH, Jaluria Y, Tewari SS. Mixed convection transport from an isolated heat source module on a horizontal plate. J Heat Transfer 1990;112:653–61.

[12] Young TJ, Vafai K. Convective cooling of a heated obstacle in a channel. Int J Heat Mass Transfer 1998;41:3131–47.

[13] Anderson AM, Moffat RJ. The adiabatic heat transfer coefficient and the superposition kernel function: Part 1—Data for arrays of flatpacks for different flow conditions. J Electronic Packaging 1992;114:14–21.

[14] Kelkar K M, Choudhury D. Numerical prediction of periodically fully developed natural convection in vertical channel with surface mounted heat generating blocks. Int J Heat Mass Transfer 1993;36:1133–45.

[15] Garimella SV, Eibeck PA. Heat transfer characteristics of an array of protruding elements in single-phase forced convection. Int J Heat Mass Transfer 1990;33:2659–69.

[16] Souza Mendes PR, Santos WFN. Heat transfer and pressure drop experiments in air-cooled electronic-component arrays. J Thermophysics and Heat Transfer 1987;1:373–8.